Designing high-temperature oxidation-resistant titanium matrix composites via directed energy deposition-based additive manufacturing

**Kellen D. Traxel**, **Amit Bandyopadhyay**[*]

W. M. Keck Biomedical Materials Research Laboratory, School of Mechanical and Materials Engineering, Washington State University, Pullman, WA 99164, USA

Abstract

Composite material development via laser-based additive manufacturing offers many exciting advantages to manufacturers; however, a significant challenge exists in our understanding of process-property relationships for these novel materials. Herein we investigate the effect of input processing parameters towards designing an oxidation-resistant titanium matrix composite. By adjusting the linear input energy density, a composite feedstock of titanium-boron carbide-boron nitride (5 wt% overall reinforcement) resulted in a highly reinforced microstructure composed of borides and carbides and nitrides, with variable properties depending on the overall input energy. Crack-free titanium-matrix composites with hardness as high as 700 ± 17 HV$_{0.2/15}$ and 99.1% relative density were achieved, with as high as a 33% decrease in oxidation mass gain in the air relative to commercially pure titanium at 700 °C for 50 h. Single-tracks and bulk samples were fabricated to understand the processing characteristics and *in situ* reactions during processing. Our results indicate that input processing parameters can play a significant role in the oxidation resistance of titanium matrix composites and can be exploited by manufacturers for improving component performance and high temperature designs.

Graphical Abstract
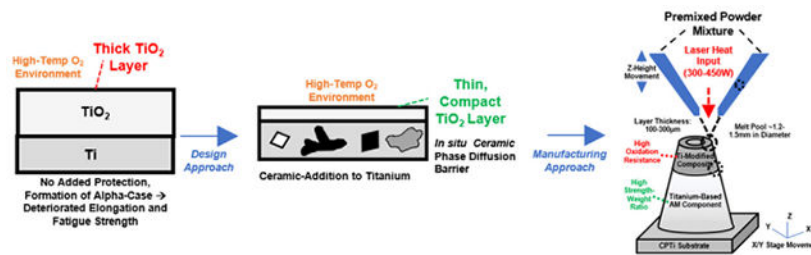
[*]Corresponding author. amitband@wsu.edu (A. Bandyopadhyay).

Declaration of Competing Interest

The authors declare that they have no known competing financial interests or personal relationships that could have appeared to influence the work reported in this paper.

1. Introduction

Continuously increasing design requirements for high-temperature applications typically require solutions that involve hybrid and advanced manufacturing strategies to develop materials and processes capable of meeting the right combination of properties and production cost for manufacturers. While traditional manufacturing approaches have proven successful in designing new high-temperature alloys and materials, additive manufacturing (AM) approaches are opening a new array of methods for fabricating and designing new materials and structures for dynamic applications [1,2]. One specific area is the development of novel metal-matrix composites for increased strength and corrosion resistance, primarily in the area of titanium-based materials [3,4]. The demand for these materials arises primarily from titanium's lack of wear resistance and strength compared to other superalloys and titanium aluminides in specific application spaces or operating environments [23]. Despite these characteristics, titanium's low density relative to the Ni-based superalloys motivates the investigation of careful enhancement of its properties by adding ceramic reinforcement, which can be leveraged by AM technology. Due to the high energy and rapid solidification nature of AM, as well as the ability to change feedstock materials with ease using directed-energy-deposition (DED, powder flow), high-temperature interactions typically occur between titanium and feedstock materials, resulting in reinforcing phases that contribute to increased properties over titanium alone (see Fig. 1A which highlights the materials employed in the current work). For example, Wang et al. (2018) investigated the variable size distribution of TiC reinforcement to titanium via DED, which resulted in variable microstructures with high tensile strength and elongation [5]. Xia et al. (2017) fabricated *in situ* TiB + TiC reinforced titanium via powder-bed-fusion of Ti/B_4C composite powder feedstocks, providing detailed analysis of the *in situ* microstructure formation and interaction zone between the titanium and ceramic reinforcement [6]. Further, Gupta et al. (2018) investigated *in situ* B_4C/BN reinforced Ti6Al4V composites. The main focus was the wear performance, with reinforcement decreasing the sliding COF by as much as half in comparison to the Ti6Al4V matrix [7].

However, one area that has seen limited attention is the high-temperature oxidation performance of these composite systems compared to titanium and other alloys, one of titanium's main limiting characteristics at temperatures above ~400 °C. Avila and Bandyopadhyay (2018) demonstrated that as high as 6 wt% BN-reinforcement in titanium, processed via directed energy deposition (DED) technology, could significantly increase the oxidation performance at very elevated temperatures (1000 °C) [8]. Further, Traxel and Bandyopadhyay (2020) demonstrated that a combination of B_4C and BN in an overall 5 wt% reinforcement amount combined high strength, hardness, wear resistance, and high-temperature oxidation resistance in comparison to the titanium matrix across a wide range of temperatures [9]. Ma et al. (2019) investigated reinforcement of TiAl-based material with TiC at variable processing parameters (via powder-bed-fusion based AM) and demonstrated

significantly increased oxidation resistance at variable processing parameters owing to the unique strengthening and multi-layer oxide film that was created [10]. These works have shown that not only can ceramic reinforcement enhance properties such as strength, hardness, and wear resistance, the presence of reinforcing phases can also add resistance to high-temperature oxidation due to the diffusion barrier and limited amount of free titanium able to oxidize to TiO_2 at the component-environment interface (see Fig. 1B). Despite this, one of the critical knowledge gaps regarding these materials' performance is how varying the laser input energy density can influence structures' resulting microstructure and subsequent properties. Often, manufacturers must adjust processing parameters to account for advanced geometries or production-specific needs, and variable input energy or change of parameters may deteriorate, improve, or influence the microstructure and oxidation performance at high temperature, potentially leading to degradation, performance enhancement, or failure of a component in operation. To this end, it was envisioned that variation of input processing parameters via directed energy deposition could alter the microstructure and oxidation performance of titanium-matrix composites based on the titanium-boron carbide-boron nitride system, which has previously been shown to have a unique combination of high strength, hardness, wear resistance, and high-temperature oxidation resistance in comparison to the titanium matrix (namely, CPTi-2.5 wt%B_4C-2.5 wt%BN) [9]. In this study, it was hypothesized that higher overall input energy into the material during processing (via lower scanning speeds and higher laser power) would influence the *in situ* decomposition of the reinforcing ceramic phase and contribute to increased overall oxidation resistance in comparison to samples produced at overall input energy densities as well as the titanium matrix alone. Our approach herein is novel as we incorporate non-titanium based ceramics and rely on full *in situ* reactivity to create reinforcing phases from B_4C and BN with pure titanium combined with the complexity of variable processing parameters, whereas most works involve incorporation of titanium-based ceramic phases such as TiN, TiC, and TiB_2 as a precursor material, which are more challenging materials to procure. Further, most works that study variable processing parameters focus on either microstructural characterization or mechanical properties, motivating the current investigation to broaden our understanding of the high-temperature oxidation behavior of these composites for increased industrial adoption. Further, in this study, we process a single CPTi-2.5 wt%B_4C-2.5 wt%BN composition (designed in our previous work [9]) in both single-track and bulk structures at a wide array of input energy densities to observe the effect of processing parameters on the resulting processability, microstructure, hardness, and high-temperature oxidation resistance. X-ray diffraction (XRD) coupled with high-magnification imaging via scanning electron microscopy (SEM) helped to understand the morphology and phase composition of the as-printed material, and thermogravimetric analysis (TGA) was utilized to understand the effect of processing parameters and subsequent microstructures on the oxidation performance in comparison to a commercially-pure titanium control. These methods were employed to assist in the evaluation of our hypothesis that processing parameters can influence the performance of these reactive, *in situ* composite materials processed using laser-based AM. Our results contribute towards our growing understanding of how laser-based AM can be exploited to create variable microstructures that result in tangible differences in a final performance for relevant environmental conditions and applications. It is envisioned that this work

can help manufacturers and researchers understand how processing changes can influence advanced composite material behavior and overall performance and design for laser-based AM fabricated components.

2.   Materials and methods

2.1.   Directed energy deposition processing for titanium composites

Block-type samples of size 10 mm square by 5 mm tall were processed using our Formalloy (San Diego, CA) directed energy deposition (DED) additive manufacturing system. This system maintains 2–4 substrate movement/rotational axes and a vertical Z-axis controlled by the deposition head. The build environment is argon-filled to limit $O_2 < 20$–30 ppm and the laser is capable of 500 W and scanning speeds>2000 mm/min. Feedstock for the current work involved spherical Grade 2 Titanium powder (CPTi, GKN Powder Metallurgy, Michigan, USA) in size range 15–45 μm, B_4C granular abrasive powder (Reade Advanced Materials, Rhode Island, USA), and granular, hexagonal-BN abrasive powder ("PTX60" from Momentive Performance Materials, Waterford, NY). The ceramic powders were premixed according to the composition from our previous work [9], namely CPTi-2.5 wt%B_4C-2.5 wt %BN (henceforth CPTi-B_4C-BN) via ball milling (without milling media) for 45 min until a homogenous mixture was observed. Separate trials of printing both CPTi (control), as well as CPTi-B_4C-BN tracks and bulk samples, were carried out by loading the respective powders into a hopper and allowing an argon stream to carry the powders from a rotating disc (rotating at 0.4 rpm) connected to the powder hopper, with argon "carrier" gas held constant at 8 L/min and a shielding gas flow rate of 16 L/min. The powders are then directed via argon stream onto the (CPTi) build substrate (and subsequent melt pool), which is aimed at the focal point of the laser onto the build substrate. Parameters for single-tracks that were printed for both compositions are shown in Table 1. After analyzing the different cross-sections of the tracks, subsequent experiments were carried out at three different linear energy densities (14 Jmm^{-1}, 42 Jmm^{-1} and 54 Jmm^{-1}), as calculated via a linear energy density relationship for single-tracks elaborated on in ref. [11]:

$$Energy\ Density = \frac{P}{\upsilon m}$$

(1)

where P is the laser power (W). υ is the laser scanning speed (mm/s), and m is the powder flow rate (g/min). For this study, all powder flowrate parameters were held constant, so the so-called "linear energy density" relationship between the laser power and scanning speed is utilized (i.e., mass flowrate taken as a constant of 1 because it was held constant across laser power and scanning speed), and units of Jmm^{-1} are used to relate the overall energy input to the processing characteristics, microstructure, and oxidation performance of the composites. The powder flow rate was held constant by maintaining constant rotational speed on our powder hopper and constant carrier gas flowrate that delivers the powder from the rotating drum to the focal point through the gas lines. Each of the nine tracks for each composition was processed ~5 mm away from one another to avoid fusion zone, and heat-affected-zone overlap during processing. After initial single-tracks were analyzed, the three separate linear energy density CPTi-B_4C-BN samples (14 Jmm^{-1}, 42 Jmm^{-1}, and 54 Jmm^{-1}) were all processed into 5 mm-tall samples with a hatch spacing of 0.8 mm (~33% overlap from

track-to-track) and an alternating 45° scanning strategy at each of the individual input energy densities, as shown in Table 1. These samples were chosen as they span the range of energy densities exhibited during processing while reducing the overall amount of samples required for full-scale analysis via TGA. Three individual samples were produced at each of the processing parameters, and all were cut from the CPTi substrate using a bandsaw cutter (around each sample), and a diamond saw cutter for sectioning and TGA sample preparation (cuts through samples).

2.2. Microstructure characterization, phase analysis

All single tracks, as well as the subsequent samples built at variable energy density, were cut from a bandsaw, mounted in acrylic resin, and sectioned via a diamond saw cutter. The cross-section of these samples was then ground using 80–2000 grit silicon carbide grinding paper. Polishing was subsequently performed on a polishing pad via alumina-DI water suspension from 1 to 0.05¼. X-Ray Diffraction (XRD) (X'Pert PRO PANalytical, Almelo, Netherlands, Cu Kα source and a Ni filter) was performed on the top surface of as-printed bulk specimens at different input energy densities in addition to the as-processed CPTi. Peaks were normalized by the largest peak observed in the spectra. Vickers cross-section hardness indents (Phase II, Upper Saddle River, NJ) were taken in line with ASTM standards on unetched cross-sections that were ground and polished, including as-oxidized samples that were tested via TGA [12,13]. High-mag imaging was performed via Field-Emission Scanning Electron Microscopy (FESEM, SEM) on etched as-printed as well as as-oxidized specimens (submersion for the 20 s in Kroll's Reagent (46 mL DI Water, 3 mL HNO_3, & 1 mL HF).

2.3. Thermogravimetric analysis (TGA)

Weight-gain measurements due to oxidation of both the control (CPTi) and variable input energy composite CPTi-B_4C-BN samples were performed via Netsch STA 409-PC Luxx (Burlington, MA). Two individual samples from each processing parameter were ground with 80-grit SiC paper and cut into 3 mm cubes for testing at 700 °C for 25 and 50 h. Before testing, each sample was loaded into a corundum (alumina) crucible equipped with a lid with a middle hole. Each sample was weighed before testing, and during each test, dynamic weight change was observed under an airstream of 0.5 psig and a 40 mL/min flow rate. Measurement during testing of the weight change was accomplished to an accuracy of 0.01 mg. For all samples, an initial heating rate of 20 °C/min was employed up until 700 °C, with hold times of 25 h and 50 h, and a subsequent 40 °C/min cooling rate was applied to reach room temperature. The surface scale was analyzed using optical and SEM imaging and high-magnification SEM imaging of the as-oxidized cross-sections and scale. Oxidation rates were analyzed according to the fundamental mass change relationship:

$$\left(\frac{\Delta W}{A_s}\right)^n = K_{l,\,p}t \qquad (2)$$

where W represents the mass gain over time, A_s the sample surface area, and $K_{l,p}$ is the rate constant given in units of ($mgcm^{-2}s^{-1}$) for linear kinetics where n = 1, and units of ($mg^2cm^{-4}s^{-1}$) for parabolic kinetics where n = 2. In the present study, at the

given oxidation conditions, all samples exhibited parabolic-breakaway kinetics. Because samples were processed at both 25hrs and 50hrs, the rate constants are provided in the average and standard deviation for each variable input parameter, as shown in Table 2. It is noted that the ranges by which the rate constants were evaluated were shortened for the CPTi-50hrs and CPTi-B_4C-BN-50hrs composition processed at 42 Jmm^{-1} due to the deviation from parabolic behavior in certain times of the test (so-called rapid increases/decreases in oxidation mass gain), as shown in Fig. 7.

3. Results

A CPTi-B_4C-BN composite composition was successfully processed into single tracks at nine different processing conditions with a wide array of input energy density. A range of three input energies (namely, 14, 42, and 54 Jmm^{-1}) were chosen to be processed into bulk samples for microstructural characterization and thermal oxidation testing and analysis to evaluate the effect of variable input energy density on the microstructure and properties of these materials for high-temperature applications.

3.1. Processing of composite single-tracks and bulk samples

Input energy density and the addition of boron carbide and boron nitride played a significant role in processing single-track and bulk samples. Cross-sectional SEM images of single-tracks of processing parameter sets shown in Table 1, increase in the fused area above the substrate and the outlines of the heat-affected zone (HAZ) occurs with increasing energy input. The HAZ depths increase as 382 μm → 560 μm → 709 μm for the input energy densities of 14, 42, and 54 Jmm^{-1}, respectively, indicating increased heat input and higher temperatures reached within the substrate (corresponding β-transus near 882 °C). For the 54 Jmm^{-1} input energy density, the HAZ outlines are barely visible at the present magnification. Comparatively, for the CPTi-B^{4}C-BN composition, the HAZ depths increase as 426 μm → 605 μm → 766 μm for the input energy densities of 14, 42, and 54 Jmm^{-1}, respectively, indicating increased heat input and higher temperatures reached within the substrate relative to the CPTi composition alone. Fusion zone (FZ) outlines were visible for the CPTi-B_4C-BN composition, and they tended to increase with increasing energy density. These FZ outlines were not visible for the CPTi composition, likely due to the smooth compositional transition from as-printed material to substrate. B_4C and BN particles were observed in each of the single tracks of the CPTi-B_4C-BN composition, with higher magnification images showing the relative reaction zones around each of the particles (Fig. 2B). For the CPTi-B_4C-BN composition processed at 14 Jmm^{-1}, limited reaction layers were exhibited, whereas in comparison, the compositions processed at 42 and 54 Jmm^{-1}, exhibited distinct reaction layers surrounding the reinforcing ceramic particles indicating more dissociation of the reinforcing particles at higher input energy density for the single-tracks. For the bulk-processed samples at each of the listed input energy densities, smooth interfaces were observed for the transition from CPTi substrate to as-printed material (Fig. 3). Near the interface, B_4C and BN particles were homogeneously dispersed. Some lack of fusion (LOF) pores were observed at low magnification, and B4C and BN particles were homogenous in the 14 Jmm^{-1} compositions. The relative amount of B_4C and BN

particles decrease substantially when increasing the input energy density, with primarily small partially-reacted particles being the key defining low-magnification feature.

3.2. Microstructure, phase analysis, hardness, and relative density

Representative microstructures of the different processing parameter sets are shown in Fig. 4. All microstructures were free from large-scale cracking and fractures between the titanium matrix and reinforcing phases. In both cases, the either coarse or fine predominant microstructure of TiN was observed, with partially-reacted particles spread homogeneously throughout. The partially-reacted BN particles exhibited TiN dendrite formation surrounding them, whereas the B_4C reaction layers consisted mainly of TiB_2 with TiB needles growing outward and granular TiC particles between the boride needles. Comparatively, at low input energy (Fig. 4A1 & 4A2), the reaction layer surrounding the B_4C particles was relatively thin (submicron), whereas, at higher input energy (Fig. 4B1 & 4B2), the reaction layer surrounding the B_4C particles was closer to 2–3 μm, indicating that at higher input energy densities there is more propensity to form the *in situ* phases. XRD analysis (Fig. 5) confirmed the presence of the predominant TiN phase (ICDD: 98.018–3415), along with the α-HCP (ICDD: 00–044-1294) matrix in the sample processed at 54 Jmm^{-1}; however, the TiN phase was not found in the sample processed at the lower input energy density of 14 Jmm^{-1}.

Differences in the microstructures regarding *in situ* reactive morphology are also characterized by the partially-reacted particle size, microhardness, and relative density of each sample at different processing parameters. Particle size distributions of the $B_4 > C$ partially-reacted particles are shown in Fig. 6A and the BN particles in Fig. 6B, comparing the high and low input energy samples (14 Jmm^{-1} and 54 Jmm^{-1}) produced with the CPTi-B_4C-BN composition. For both of the ceramic partially-reacted particles, there is a clear shift in the overall distribution when considering as-sieved powder and as-printed partially-reacted particles in the microstructure. For the B_4C particles in the as-processed microstructure for 14 Jmm^{-1}, there were ~60% of particles between the size of 30–50 μm, whereas the B_4C particles in the as-processed microstructure for 54 Jmm^{-1} exhibited nearly ~75% of particles between the size of 10–30 μm, with heavy low-end weighting compared to both other distributions, indicating a proportionate amount of smaller partially-reacted particles in the microstructures of higher-energy input samples in comparison to lower input energy, as well as the as-sieved powders. Much more overlap was observed for the BN particles where nearly ~80% of particles between the size of 40–75 μm were observed for the as-processed microstructure at 14 Jmm^{-1}, and nearly ~70% of particles between the size of 35–75 μm at 54 Jmm^{-1}, indicating significant overlap. In terms of the overall area fraction of partially-reacted particles in the microstructure, however, there was a significant decrease in area fraction when comparing the different input energy densities as the area fraction decreased by 75% from 1.67% to 0.41% for the B_4C particles when comparing 14 Jmm^{-1} and 54 Jmm^{-1}, and 51% decrease from 3.47% to 1.7% for the BN particles when similarly comparing 14 Jmm^{-1} and 54 Jmm^{-1}. Hardness and relative density measurements for each of the processing conditions are shown in Fig. 7. For all compositions, there was no clear trend in hardness when considering indents taken near the interface (or "base"), the bulk of the structure ("middle"), or near the top of the sample itself ("top"),

indicating that heat accumulation that occurs during processing is not a contributing factor to the resulting microstructure as much as the initial processing parameters themselves and presence of the ceramic reinforcement. However, there is a nearly 60% increase in hardness when considering the bulk values from the processing inputs of 14 Jmm^{-1} to 54 Jmm^{-1}, i.e., an increase from 440 ± 23 $HV_{0.2/15}$ to 700 ± 17 $HV_{0.2/15}$. The sample produced at the intermediate 42 Jmm^{-1} exhibited an intermediate hardness of 549 ± 20 $HV_{0.2/15}$ Comparatively, as-printed CPTi maintained an average hardness of 273 ± 14 $HV_{0.2/15}$, nearly 39% of the hardness exhibited in the reinforced composition at 54 Jmm^{-1}. Further, relative density was also increased with the increased energy input, namely, as high as $99.6 \pm 0.5\%$ relative density was achieved in the reinforced composition processed at 54 Jmm^{-1}. Comparatively, the compositions processed at 14 Jmm^{-1} and 42 Jmm^{-1} maintained high relative densities of $98.0 \pm 0.2\%$ and $99.1 \pm 0.2\%$, respectively. For reference, as-printed CPTi had a relative density of $98.3 \pm 0.3\%$, indicating that each composition's processing and strategy choices result in quality densification, despite different microstructure features.

3.3. Isothermal oxidation

Processing parameters also played a significant role in improving the oxidation behavior of the CPTi-B_4C-BN composition compared to the CPTi composition. Fig. 8 highlights the thermogravimetric curves of each of the compositions and processing parameters associated with the CPTi-B_4C-BN composition, with associated rate constant values for each parabolic fit. For each of the CPTi-B_4C-BN samples processed at variable parameters, there is an apparent decrease in the overall oxidation mass gain and the rate constant throughout the 50hr test compared to the control of CPTi. While there is added improvement in decreasing the mass gain with increased input energy density from 14 Jmm^{-1} to 42–54 Jmm^{-1}, there is not much improvement when comparing the 42 Jmm^{-1} and 54 Jmm^{-1} thermogravimetric curves. The inset image shows the end values of the normalized mass gain over the 50hr test. An ~33% decrease is observed when comparing the end values of CPTi to the CPTi-B_4C-BN compositions processed at both 42 Jmm^{-1} and 54 Jmm^{-1} (from ~0.975 $mgcm^{-2}$ to ~0.65 $mgcm^{-2}$), with an ~20% decrease observed when comparing the end values of CPTi to the CPTi-B_4C-BN compositions processed at 14 Jmm^{-1} (from ~0.975 $mgcm^{-2}$ to ~0.775 $mgcm^{-2}$). The rate constant decreases observed similar improvements in oxidation resistance (see Table 2), with each of the n-values between 1.38 and 1.44 (indicating a mixed parabolic-breakaway kinetic regime), but a significant difference was observed between the rate constant parameters themselves. More specifically, a 16% decrease in the overall average rate constant was observed when comparing the CPTi and the CPTi-B_4C-BN composition processed at 14 Jmm^{-1} (from $6.55e^{-2}$ to $5.53e^{-2}$, and as high as 34–55% decreases were observed for the CPTi-B_4C-BN compositions processed at 42–54 Jmm^{-1}, with some of the variations in that processing range attributed to the parabolic-breakaway kinetics which can affect the parabolic fit that is applied to the dataset for analysis.

Improvements in oxidation performance were also evidenced from micrographs of the oxide scale, as shown in Figs. 9 and 10. The CPTi exhibited extensive oxide scale growth at 25 h, resulting in a uniform layer of crystals, as shown at high magnification. After 50hrs, the scale became more widespread in addition to growing outward from the surface, with TiO_2 crystals on the order of 5–10 μm in size protruding from the material's surface.

Comparatively, both of the CPTi-B_4C-BN compositions exhibited scattered oxide crystal nucleation across the surface at 25 h of testing, with localized scales much smaller in comparison to the highly-spread CPTi composition. At 50hrs, the scale grew and maintained crystallites in both processing parameter sets in the submicron scale, indicating highly stunted oxide growth compared to the CPTi composition. Comparing the CPTi-B_4C-BN composition between both processing sets, there was no apparent effect of the input energy on the overall scale morphology or characteristics, with both having scattered nucleation at 25 h and then submicron crystallite growth at 50hrs of testing. Further, each of the CPTi-B_4C-BN compositions had compact oxide scales nearly 50% thinner than that of the CPTi composition after 50hrs (see Fig. 10). More specifically, CPTi had a scale thickness of 4.11 ± 0.15 μm, and the CPTi-B_4C-BN composition had scale thicknesses of 1.81 ± 0.21 μm and 1.62 ± 0.35 μm when processed at 14 Jmm$^-$ and 54 Jmm^{-1}, respectively. However, the microstructures differed as the CPTi-B_4C-BN composition processed at 14 Jmm^{-1} exhibited a networked/cellular TiB morphology, and the composition processed at 54 Jmm^{-1} exhibited a more needle-like TiB morphology, with highly coarsened needles on the order of 10–15 μm in size near the oxide scale. Fig. 11A shows the hardness of each composition at different processing parameters after each of the separate tests. For the CPTi-B_4C-BN composition processed at 14 Jmm^{-1}, there was a 9% increase in average bulk hardness from 463 ± 16 HV$_{0.2/15}$ in the as-processed state to 506 ± 11 HV$_{0.2/15}$ after 50hrs of testing. Comparatively, for the CPTi-B_4C-BN composition processed at 42 Jmm^{-1}, there was 5% increase in average bulk hardness from 551 ± 20 HV$_{0.2/15}$ in the as-processed state to 580 ± 27 HV$_{0.2/15}$ after 50hrs of testing. And then finally for the CPTi-B_4C-BN composition processed at 54 Jmm^{-1} there was a 4% increase in average bulk hardness from 637 ± 12 HV$_{0.2/15}$ in the as-processed state to 662 ± 19 HV$_{0.2/15}$ after 50hrs of testing, indicating slight increases in hardness and continued *in situ* reactivity of the composites under extensive testing, but not of a significant nature. Further, the micrographs in Fig. 11B & 11C show the high-magnification microstructures of the CPTi-B_4C-BN compositions at different processing parameters after 50hrs of testing. Microstructures at both input energies of 14 Jmm^{-1} and 54 Jmm^{-1} exhibited similar morphologies to the micrographs shown in Figs. 2–4, with BN particles ranging in size from 30 to 75 pm and B_4C particles in the range of 20–55 μm, with the presence of these particles shown more prominently at lower input energy was observed in the as-processed state. These particle sizes align with the distribution of particle size in the as-processed state (Fig. 5), further indicating a limited amount of increased reactivity of the titanium matrix during high-temperature oxidation.

4. Discussion

Titanium-boron carbide-boron nitride metal-ceramic composites were successfully processed in both single tracks and bulk structures using directed energy deposition at variable input energies to understand the effects of processing inputs on the resulting microstructures and oxidation performance in comparison to titanium, which suffers from poor oxidation performance at elevated temperature. High magnification imaging coupled with X-ray diffraction and bulk property measurements aid in understanding processing parameter effects on this composite material system concerning both the microstructures and the oxidation performance.

4.1. influence of processing parameters on microstructures

Laser-based directed energy deposition is a complex transient-thermal process whose processing parameters greatly influence the resulting microstructures that form, especially when the feedstocks themselves are interacting during processing. The microstructures that form both within the bulk and near the outline of the ceramic-titanium interface can be understood from looking at the Gibbs Free Energy change of reactions within the Ti-BN and Ti-B_4C system [9]. More specifically, the key exothermic reactions $G < 0$ across wide temperature range) that have been reported previously for these material systems are as shown [14–17]:

$$5Ti + B_4C \rightarrow 4TiB + TiC \tag{3}$$

$$3Ti + 2BN \rightarrow TiB_2 + 2TiN \tag{4}$$

$$Ti + TiB_2 \rightarrow 2TiB \tag{5}$$
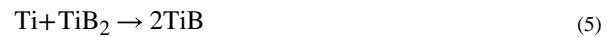
Eqs. (3) and (4) adequately describe the formation of TiB_2, TiB, TiC, and TiN from the premixed feedstocks of titanium, B_4C, and BN, and Eq. (5) describes the formation of TiB in an abundance of titanium from the TiB_2 periphery reaction layer surrounding B_4C particles, which has been previously evaluated in related work with similar titanium-based composite material systems [6,18]. From the XRD analysis, only TiN was able to be explicitly identified in the bulk composition processed at 54 Jmm^{-1}, despite direct comparison of the formation of TiB_2/TiB, and TiC as previously evidenced in other studies of similar overall composition [9,19–21], which is attributed to both significant overlap in peaks for these phases within the main 35-40° 2Θ range as well as the small scale of the *in situ* reinforcing phases themselves. Despite this fact, the TiN dendritic structures appeared more coarsened and prominent (shown in Fig. 4B1) when processed at 54 Jmm^{-1}, in comparison to the fine TiN dendrite morphology when processed at 14 mm^{-1}, which helps substantiate that the TiN phase could be explicitly identified at 54 Jmm^{-1} and not at 14 Jmm^{-1} in the XRD analysis. This coarsened microstructure is directly related to increased time for diffusion (500 mm/min scanning speed vs. 1500 mm/min scanning speed) and increased input power, which leads to higher mobility for the decomposition of the ceramic particles within the titanium matrix. This increased decomposition was also observed in the high-magnification images of the single tracks (Fig. 2B), where increased reaction layers were observed. While the decomposition shown in the single track does not directly lead to the microstructures observed in the bulk samples, the general similarities in morphologies at different input energies between the single tracks and bulk structures indicates the propensity of single tracks to evaluate microstructural differences of the same composition processed under different processing parameters, without the need for building bulk samples.

Further, increased energy density resulted in a ~50–75% decrease in the overall area fraction of partially reacted particles, with significant particle size and area shift compared to the as-sieved powders. There are varying degrees of overlap when comparing the B_4C and BN

particle sizes and areas when processed at different conditions, indicating that similar overall reaction zone size-distributions are occurring at different processing parameters in regions of partial-reaction, even if the overall amount of decomposition increases with increasing input energy. Additionally, the smaller overall area fraction of partially-reacted B_4C particles in comparison to the BN (Fig. 6C) as well as shifted partially-reacted particle size and area in comparison to BN (Fig. 6A & B) is likely related to the difference in G for the reactions between the different feedstock constituents, i.e., the reaction from Eq. (3) for B_4C with titanium results in a $\Delta G = -798\frac{KJ}{mol}$, whereas Eq. (4) related to the reactions of BN with titanium results in a $\Delta G = -504\frac{KJ}{mol}$. More specifically, the lower free energy change associated with the B_4C reactions results in differences in the reactivity of the ceramic constituents with the titanium matrix compared to BN.

The increase in input energy density's effect on the resulting microstructures is also positively related to increases in the microstructural hardness and densification behavior (Fig. 7A & 7B), compared to other titanium-matrix composite material systems studied in the literature. Xia et al. (2017) reported hardness of a Ti-TiB-TiC composite at 577 $HV_{0.2}$ at 5 wt% overall reinforcement amount [6], and Gupta et al. (2018) reported hardness in the range of 450–600 HV for 5 vol% reinforcement, with the lowest relative porosity of > 30% [7], indicating the present study's efficacy to create high quality (>99% density), crack-free composite titanium materials with hardness in the range of 460–640 HV by adjusting the input processing parameters to influence the *in situ* reactions that occur during processing. Because of the exothermic reaction nature of this material system, the increases in densification are likely due to both the increased effective laser input energy as well as the increased energy that occurs from the decomposition of the ceramic phase during processing, resulting in more melting and remelting of the titanium matrix to increase the final as-processed relative densities.

4.2. Influence of processing parameters on oxidation performance

Higher input energy positively affected the normalized mass gain performance, resulting in as much as a 33% decrease in normalized mass gain for the CPTi-B_4C-BN composition processed at 54 Jmm^{-1} in comparison to CPTi, and 20% decrease in normalized mass gain for the CPTi-B_4C-BN composition processed at 14 Jmm^{-1} in comparison to CPTi. Our previous work using Arrhenius analysis with the same CPTi-B_4C-BN composition in the current study, coupled with XRD analysis of the as-oxidized surface, verified that the mass gain in this composite system when exposed to elevated temperatures in air is due to the formation of rutile (TiO_2) on the surface [9]. The difference between the formation of this oxide scale at variable processing parameter sets in the current study is directly attributed to the increased amount of TiN *in situ* formation and predominance in the microstructure at higher input energy, which has been shown previously to positively affect both the kinetics and overall mass gain in comparison to titanium [9]. With more TiN formation at increased energy density, the improvement to the oxidation is due to both tying up titanium atoms in reinforcing phases (TiN, TiB, TiC, etc.) which reduces the ability for free titanium diffusion to the surface, as well as the increased amount of reinforcing phase that acts as a physical diffusion boundary for the titanium atoms in the microstructure. This phenomenon

has also been shown in Ma et al. (2019), but because Ti6Al4V alloy was used as the matrix, there was both a diffusion barrier and *in situ* reinforcing phases and a multi-layer oxide of both TiO_2 as well as Al_2O_3. Further, in the present work there was a limited increase in oxidation performance shown when processing at 42 Jmm^{-1} or 54 Jmm^{-1}, which was directly attributed to similarities in the microstructural characteristics of the *in situ* reinforcing phases, indicating that increased formation of *in situ* reinforcing phases has a limited effect on oxidation performance in this material system processed at the higher input energy density. Additionally, these compositions' similar scanning speed (500 mm/min) may indicate that scanning speed might play a more prominent role in the oxidation performance than laser power alone; however, further study is necessary to confirm this hypothesis.

Despite the difference in overall mass gain when comparing the CPTi-B$_4$C-BN composition processed at both 42 Jmm^{-1} or 54 Jmm^{-1}, there was still a clear improvement in the oxidation characteristics when looking at the microstructures and scale formation in the cross-section of the as-oxidized 14 Jmm^{-1} and 54 Jmm^{-1} input energy samples after 50hrs of testing in the air at 700 °C. Moreover, both CPTi-B$_4$C-BN compositions processed at 14 Jmm^{-1} and 54 Jmm^{-1} had compact scales (see Figs. 9 and 10) that were well-adhered to the surface and were ~50% thinner compared to the CPTi composition. At 25hrs, both scales exhibited localized scales scattered compared to the CPTi composition, which exhibited a widely-spread oxide scale with micron-scale crystallites spread throughout the entire surface. Further, while the cross-sectional microstructure of the CPTi-B$_4$C-BN composition processed at 14 Jmm^{-1} near the surface (Fig. 10) was more of a networked boride structure similar to that previously reported in TiB-Ti composites [22], and the composition processed at 54 Jmm^{-1} had more coarsened boride needles near the surface, both contributed to thinner, compact scales in comparison to the CPTi composition on its own. Further, the hardness and microstructural characteristics (partially-reacted particle size, morphology) at high magnification (see Fig. 11) indicate a limited difference in properties comparing pre-post oxidation, indicating the propensity of both processing conditions to contribute to improved oxidation performance as well as microstructural stability long term (only 5–10% increases in hardness). This limited increase in hardness and microstructural evolution was reported previously at 700 °C oxidation testing, whereas at higher temperatures (850 °C-1000 ° C), increased reactivity between titanium and the ceramic phase contributed to significant increases in hardness for several compositions like the present study. Because of the limited effect of oxidation on the microstructure and hardness for a wide range of input energy and the improvements in mass gain and oxide scale compactness, a wide range of processing conditions can contribute to increased oxidation performance in comparison to the CPTi matrix alone. This is important for manufacturers because different microstructural characteristics may lead to improved or deteriorating properties such as strength, creep, and fatigue, all relevant to the structural composite material investigated in the present study.

5. Conclusions

A CPTi-B$_4$C-BN composition was processed via laser-based additive manufacturing with variable input processing parameters to understand the influence of processing characteristics on the highly oxidation-resistant titanium matrix composite towards influencing the microstructure and properties for high-temperature applications. By

adjusting the linear input energy density, a composite feedstock of titanium-boron carbide-boron nitride (5 wt% overall reinforcement) resulted in a highly reinforced microstructure composed of borides and carbides and nitrides, with variable properties depending on the overall input energy. Crack-free titanium-matrix composites with hardness as high as 700 ± 17 HV$_{0.2/15}$, and 99.1% relative density were achieved, with as high as a 33% decrease in oxidation mass gain the air relative to titanium at 700 °C for 50hr. Single-tracks and bulk samples were fabricated to understand the processing characteristics better and *in situ* reactions that occur during processing. The CPTi-B$_4$C-BN composition exhibited excellent oxidation resistance and microstructural stability (only ~5–10% increases in hardness throughout testing at 700 °C for 50hrs) at a wide range of input energy densities, indicating that various processing parameters can be employed to achieve increased oxidation resistance in this class of materials. Our results indicate that input processing parameters can play a significant role in the microstructure formation and oxidation resistance of titanium matrix composites using laser-based additive manufacturing and can be exploited by manufacturers for improving properties of these composite material systems for high-temperature applications.

Acknowledgements

References

[1]. DebRoy T, Wei HL, Zuback JS, Mukherjee T, Elmer JW, Milewski JO, et al. , Additive manufacturing of metallic components – Process, structure and properties, Prog. Mater Sci 92 (2018) 112–224, 10.1016/j.pmatsci.2017.10.001.

[2]. Pollock TM, Clarke AJ, Babu SS, Design and Tailoring of Alloys for Additive Manufacturing, Metall. Mater. Trans. APhys. Metall. Mater. Sci (2020), 10.1007/s11661-020-06009-3.

[3]. Attar H, Ehtemam-Haghighi S, Kent D, Dargusch MS, Recent developments and opportunities in additive manufacturing of titanium-based matrix composites: A review, Int. J. Mach. Tools Manuf 133 (2018) 85–102, 10.1016/j.ijmachtools.2018.06.003.

[4]. Hayat MD, Singh H, He Z, Cao P, Titanium metal matrix composites: An overview, Compos Part A Appl Sci Manuf 121 (2019) 418–438, 10.1016/j.compositesa.2019.04.005.

[5]. Wang J, Li L, Lin P, Wang J, Effect of TiC particle size on the microstructure and tensile properties of TiCp/Ti6Al4V composites fabricated by laser melting deposition, Opt. Laser Technol 105 (2018) 195–206, 10.1016/j.optlastec.2018.03.009.

[6]. Xia M, Liu A, Hou Z, Li N, Chen Z, Ding H, Microstructure growth behavior and its evolution mechanism during laser additive manufacture of in-situ reinforced (TiB+TiC)/Ti composite, J. Alloy. Compd 728 (2017) 436–444, 10.1016/j.jallcom.2017.09.033.

[7]. Gupta A, Hussain M, Misra S, Das AK, Mandal A, Processing and characterization of laser sintered hybrid B 4 C/cBN reinforced Ti-based metal matrix composite, Opt. Lasers Eng 105 (2018) 159–172, 10.1016/j.optlaseng.2018.01.015.

[8]. Avila JD, Bandyopadhyay A, Influence of boron nitride on reinforcement to improve high temperature oxidation resistance of titanium, J. Mater. Res (2019) 1–11, 10.1557/jmr.2019.11.

[9]. Traxel KD, Bandyopadhyay A, Influence of in situ ceramic reinforcement towards tailoring titanium matrix composites using laser-based additive manufacturing, Addit. Manuf 31 (2020), 10.1016/j.addma.2019.101004101004.

[10]. Ma C, Gu D, Dai D, Zhang H, Zhang H, Yang J, et al. , Microstructure evolution and high-temperature oxidation behaviour of selective laser melted TiC/TiAl composites, Surf Coatings Technol 375 (2019) 534–543, 10.1016/j.surfcoat.2019.07.059.

[11]. Traxel KD, Malihi D, Starkey K, Bandyopadhyay A, Model-driven directed-energy-deposition process workflow incorporating powder flowrate as key parameter, Manuf Lett (2020), 10.1016/j.mfglet.2020.08.005.

[12]. ASTM Standard E384–16, Test Method for Microindentation Hardness of Materials, ASTM International, West Conshohocken, PA, PA, 2016. 10.1520/E0384-16.

[13]. ASTM Standard C1327, Test Method for Vickers Indentation Hardness of Advanced Ceramics, ASTM International, West Conshohocken, PA, PA, 2015. 10.1520/C1327-08.2.

[14]. Yi M, Zhang X, Liu G, Wang B, Shao H, Qiao G, Comparative investigation on microstructures and mechanical properties of (TiB + TiC)/Ti-6Al-4V composites from Ti-B4C-C and Ti-TiB2-TiC systems, Mater. Charact (2018), 10.1016/j.matchar.2018.04.010.

[15]. Ogunlana MO, Akinlabi ET, Erinosho MF, Analysis of the influence of laser power on the microstructure and properties of a titanium alloy-reinforced boron carbide matrix composite (Ti6Al4V-B4C), Stroj Vestnik/Journal Mech Eng (2017), 10.5545/sv-jme.2016.4159.

[16]. Zhang J, Ke W, Ji W, Fan Z, Wang W, Fu Z, Microstructure and properties of insitu titanium boride (TiB)/titanium (TI) composites, Mater. Sci. Eng., A 648 (2015) 158–163, 10.1016/j.msea.2015.09.067.

[17]. Panda KB, Chandran KSR, First principles determination of elastic constants and chemical bonding of titanium boride (TiB) on the basis of density functional theory, Acta Mater. 54 (2006) 1641–1657, 10.1016/j.actamat.2005.12.003.

[18]. Zhang Y, Sun J, Vilar R, Characterization of (TiB + TiC)/TC4 in situ titanium matrix composites prepared by laser direct deposition, J. Mater. Process. Technol (2011), 10.1016/j.jmatprotec.2010.11.009.

[19]. Traxel KD, Bandyopadhyay A, Reactive-deposition-based additive manufacturing of Ti-Zr-BN composites, Addit. Manuf 24 (2018), 10.1016/j.addma.2018.10.005.

[20]. Das M, Balla VK, Basu D, Manna I, Sampath Kumar TS, Bandyopadhyay A, Laser processing of in situ synthesized TiB-TiN-reinforced Ti6Al4V alloy coatings, Scr. Mater 66 (2012) 578–581, 10.1016/j.scriptamat.2012.01.010.

[21]. Das M, Bhattacharya K, Dittrick SA, Mandal C, Balla VK, Sampath Kumar TS, et al. , In situ synthesized TiB-TiN reinforced Ti6Al4V alloy composite coatings: Microstructure, tribological and in-vitro biocompatibility, J. Mech. Behav. Biomed. Mater 29 (2014) 259–271, 10.1016/j.jmbbm.2013.09.006. [PubMed: 24121827]

[22]. Hu Y, Cong W, Wang X, Li Y, Ning F, Wang H, Laser deposition-additive manufacturing of TiB-Ti composites with novel three-dimensional quasi-continuous network microstructure: Effects on strengthening and toughening, Compos. Part B Eng 133 (2018) 91–100, 10.1016/j.compositesb.2017.09.019.

[23]. Traxel Kellen D., Reaction-Based Laser Additive Manufacturing of Structural Metal-Ceramic Composites: Experimentation and Thermal Process Modeling, Washington State University (2021).

Author Manuscript

Author Manuscript

Author Manuscript

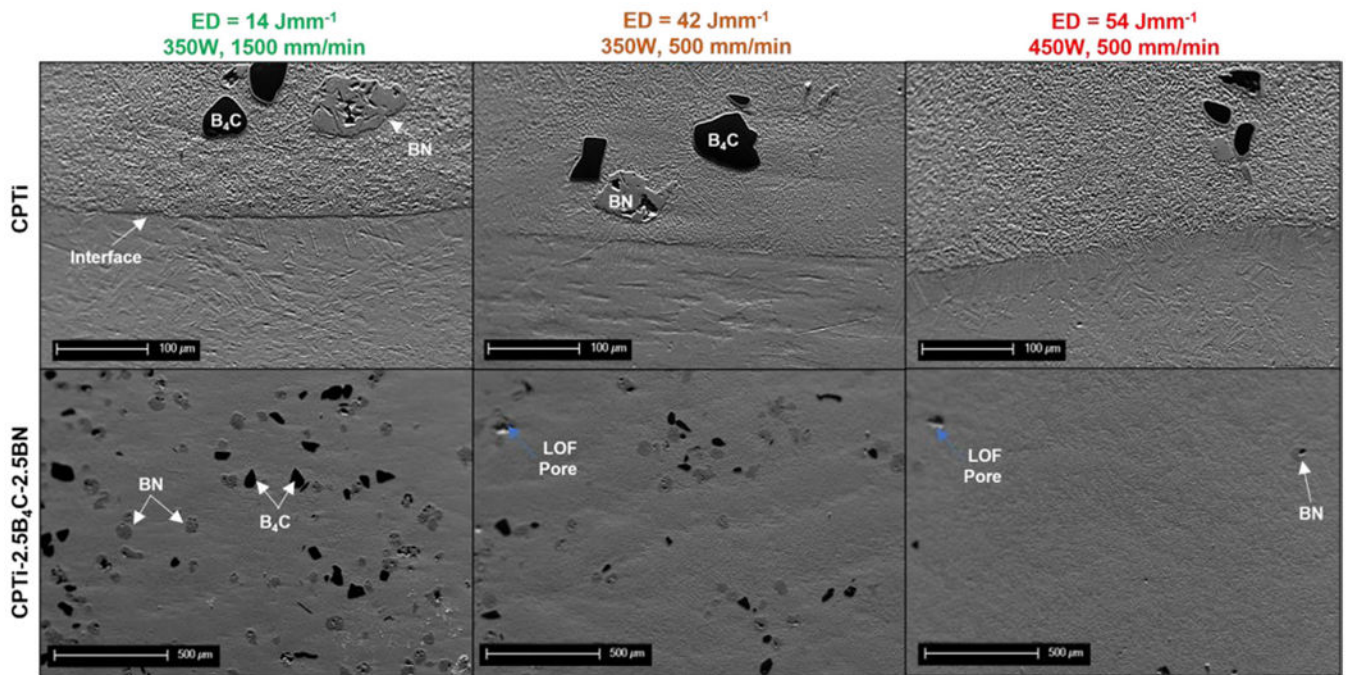Author Manuscript

HIGHLIGHTS

- Use of directed energy deposition-based additive manufacturing to design Ti-matrix composites.

- In situ ceramic reinforcement improved oxidation resistance of Ti matrix composites.

- Input energy had a significant impact on microstructure and oxidation resistance.
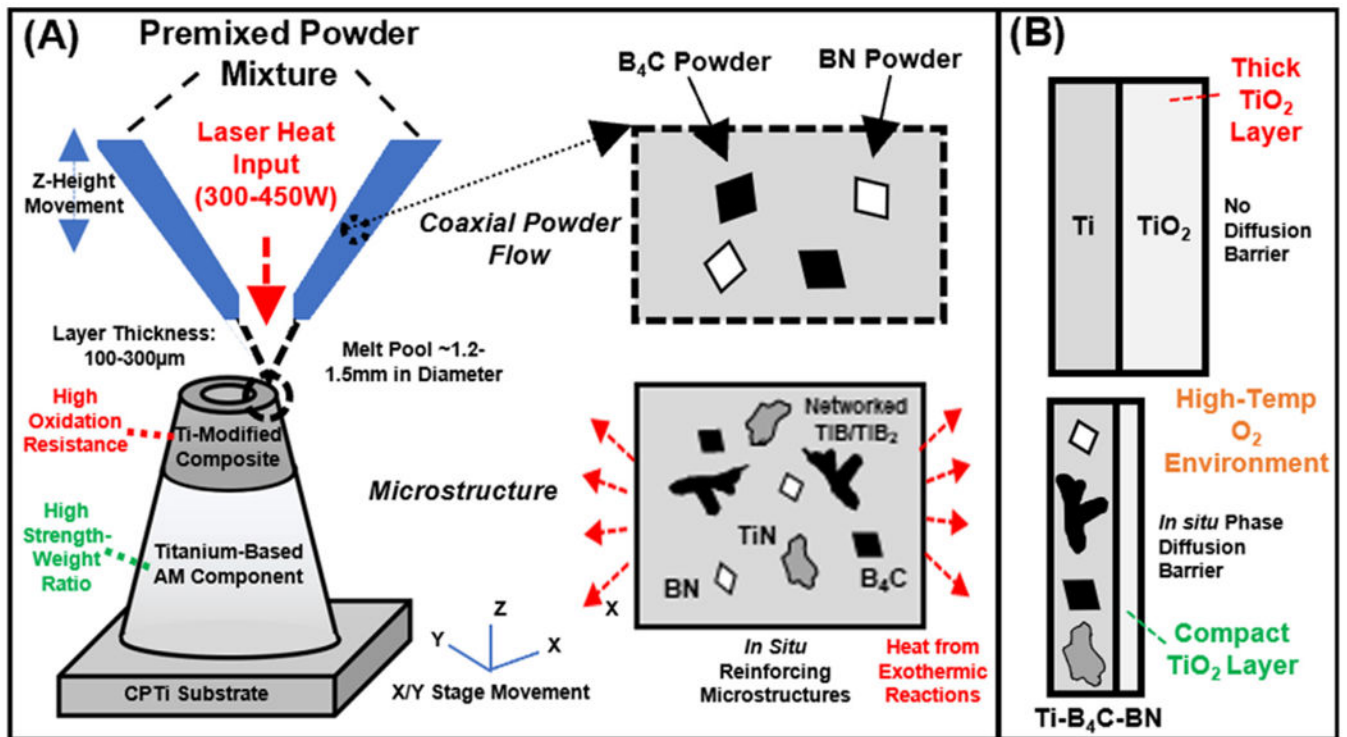
Fig. 1.
Reactive-based reinforcement concept for titanium-based components. **(A)** Processing via directed energy deposition technology (DED). **(B)** Performance improvement using ceramic reinforcement for increased oxidation resistance. Graphic reproduced from reference [23].
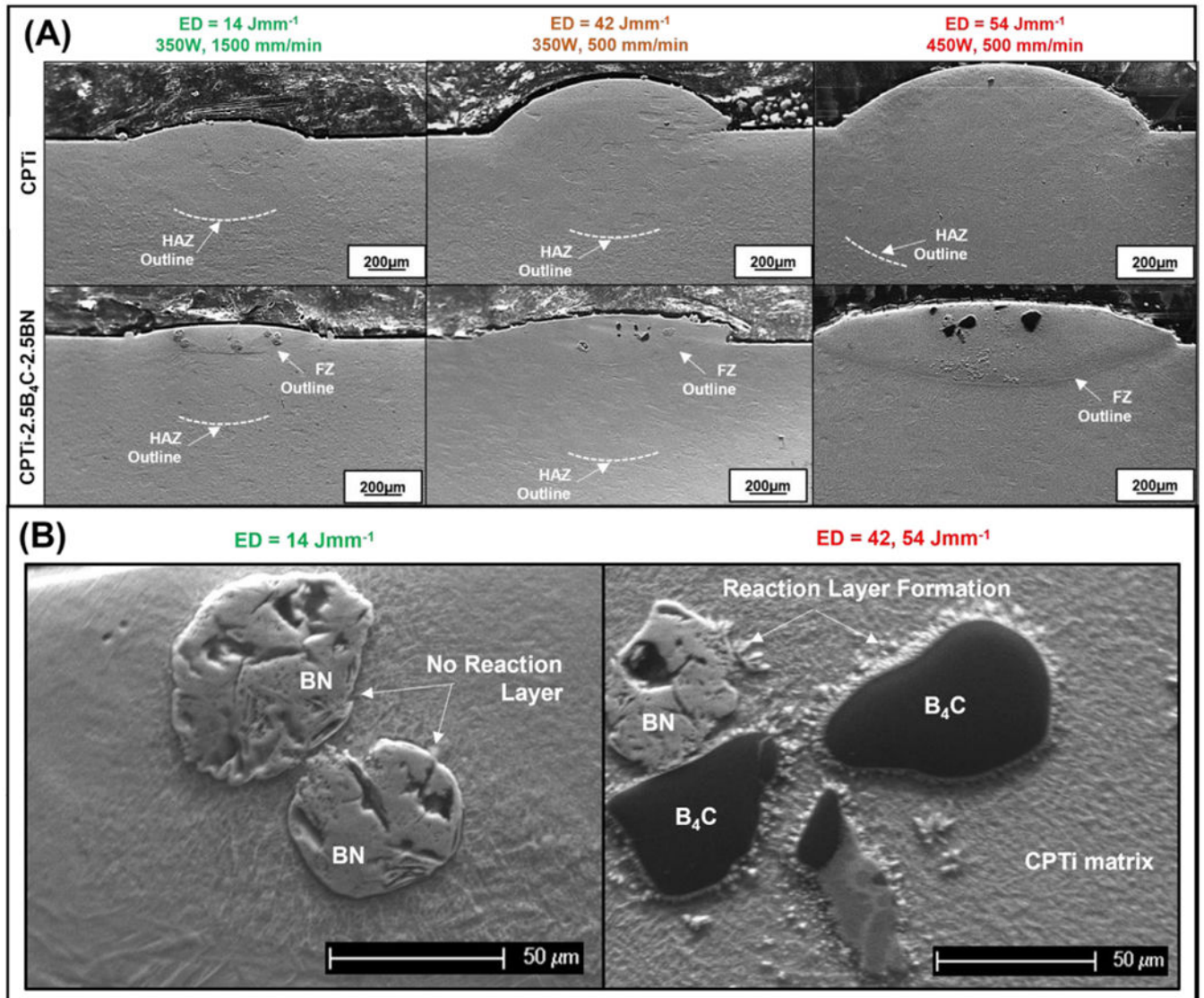
Fig. 2.
Comparison of low and high-magnification images of tracks at 14–54 Jmm^{-1} input energy density. **(A)** Single tracks of both CPTi and CPTi-B$_4$C-BN, and **(B)** Comparison of CPTi-B$_4$C-BN processed at both low and high input enery density.

Fig. 3.
Comparison of interfaces and low-magnification images of bulk samples processed at 14-54 Jmm^{-1} input energy density. **(Top Row)** CPTi, and **(Bottom Row)** CPTi-2.5B$_4$C-BN.
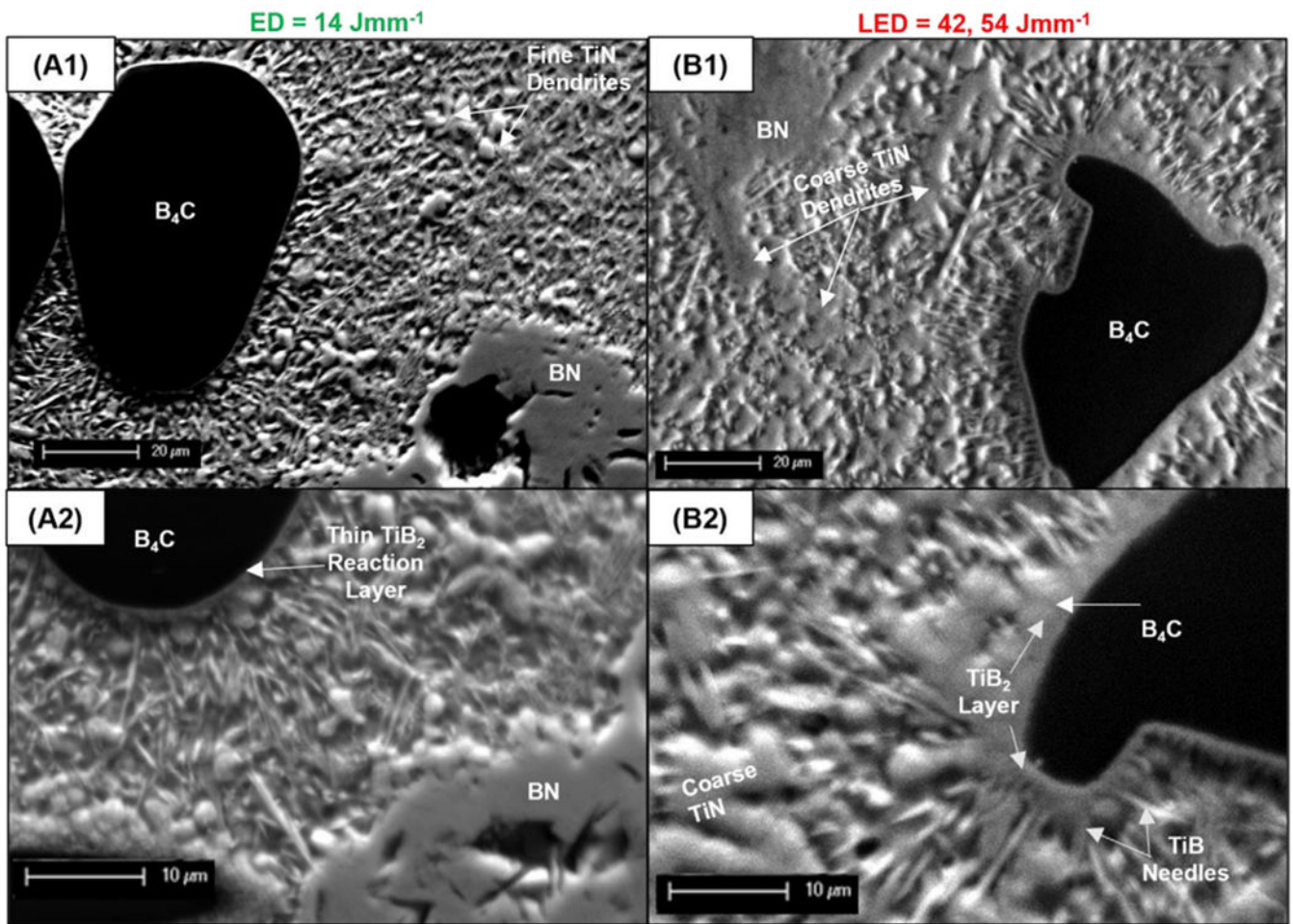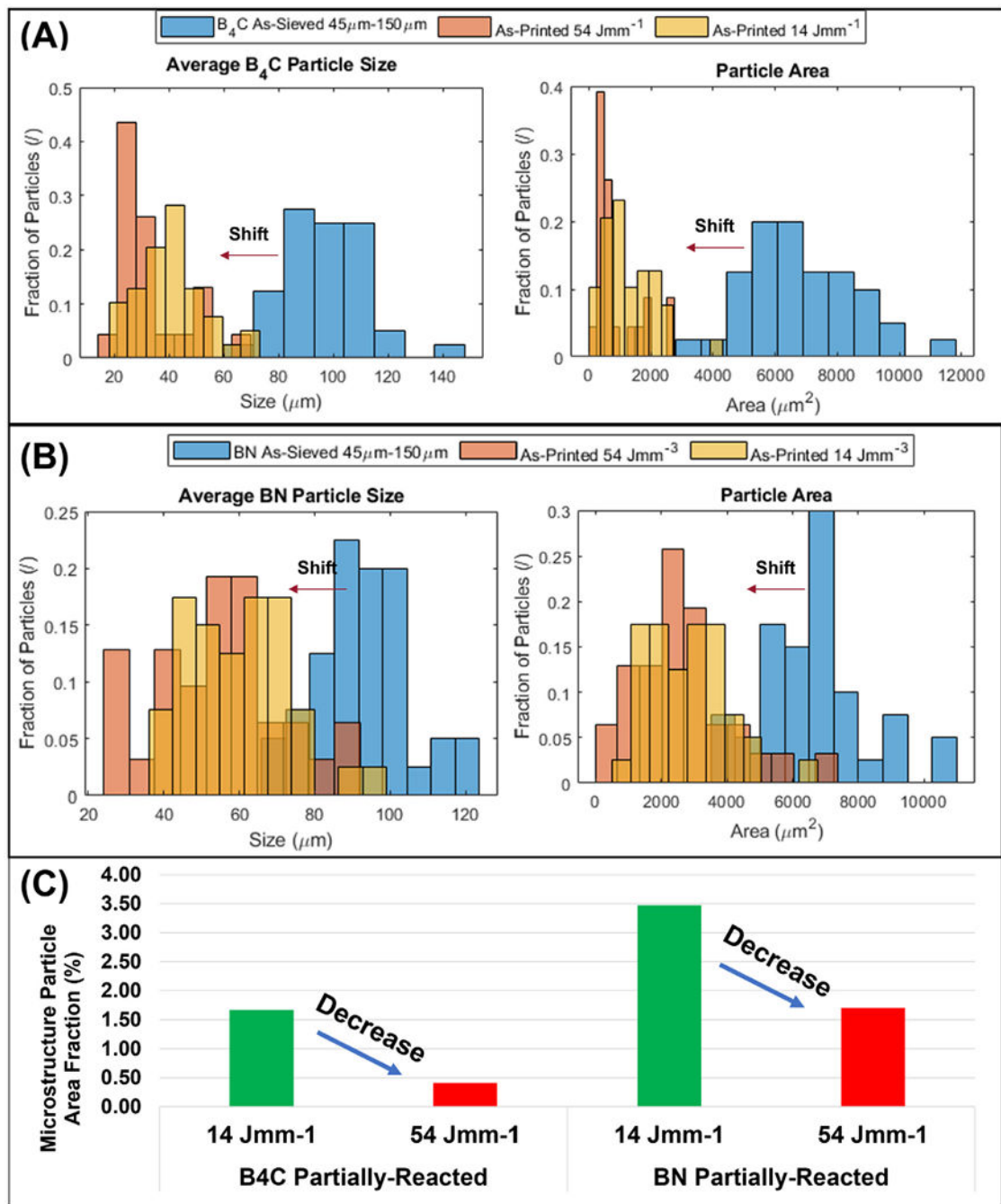
Fig. 4.
High magnification microstructures of variable process parameter samples. **(A1 & A2)**
14 Jmm^{-1} at increasing magnification, and *(B1 & B2)* 42–54 Jmm^{-1} at increasing
magnification.
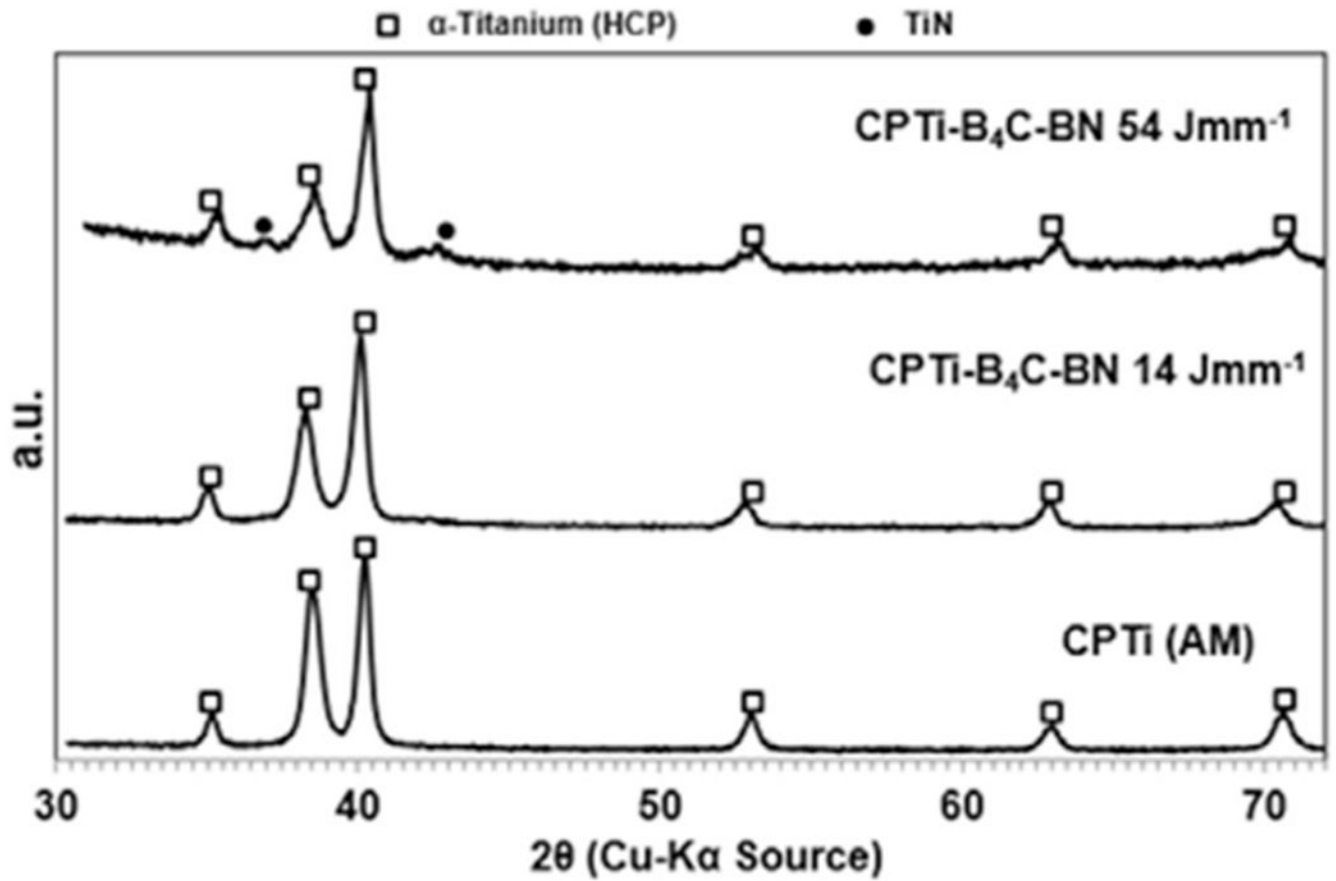
Fig. 5.
XRD analysis of as-printed CPTi and the CPTi-B_4C-BN composition processed at both low input energy (14 Jmm^{-1}) and high input energy density (54 Jmm^{-1}).

Fig. 6.
PSD distribution of B_4C and BN particles at different processing conditions in comparison to as-sieved condition. Note: 20–40 measured particles contribute to each distribution. **(A)** B_4C. **(B)** BN. **(C)** Comparison of overall area fraction of as-processed particle sizes in the microstructure for each reinforcement and processing parameter set.
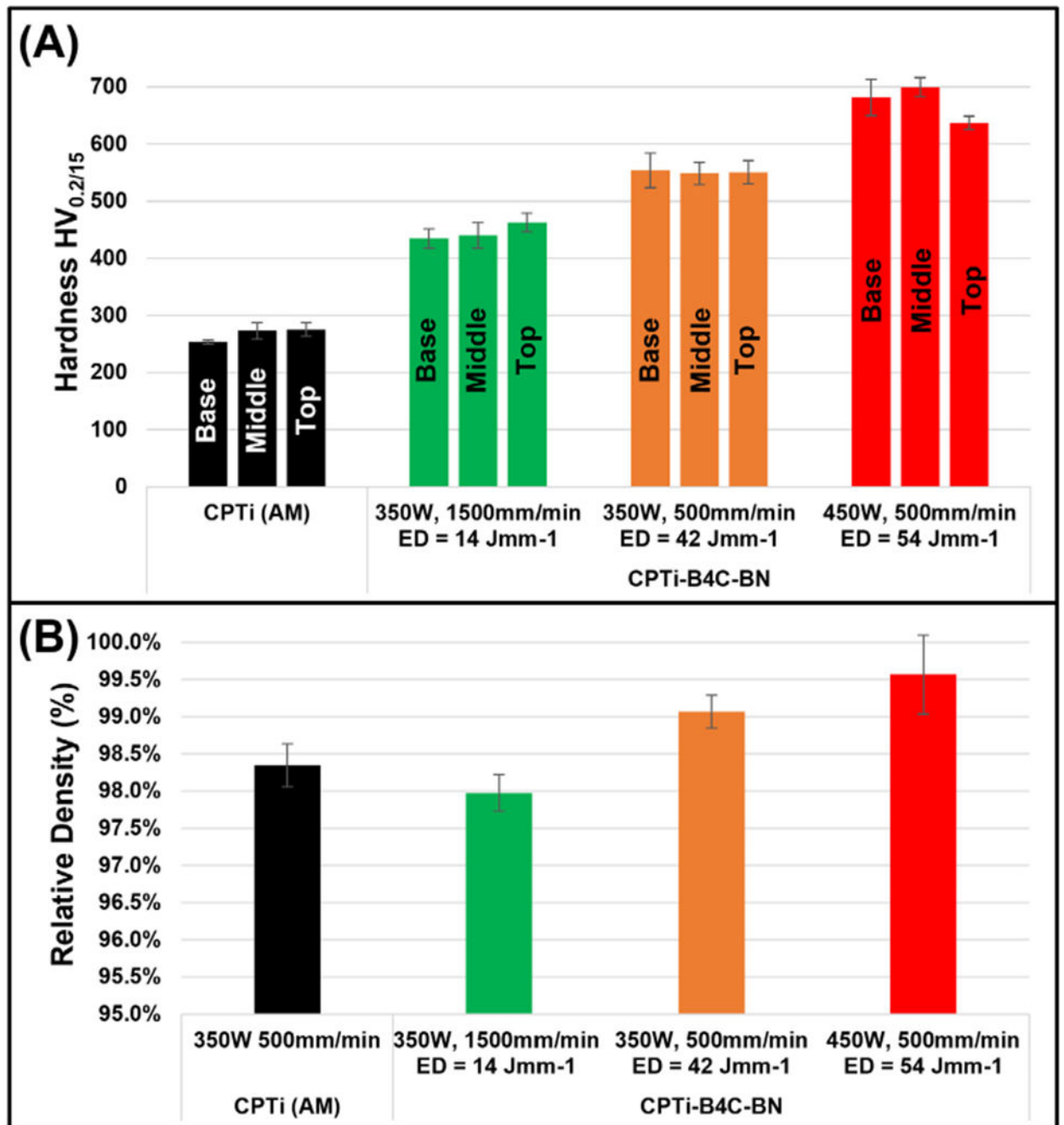
Fig. 7.
Hardness and relative density of composites at different processing conditions. **(A)** Hardness of each energy density within the base, middle, and top of the deposits. **(B)** Relative density of each energy density in comparison to CPTi. Note that relative density was calculated with respect to the theoretical composite composition.
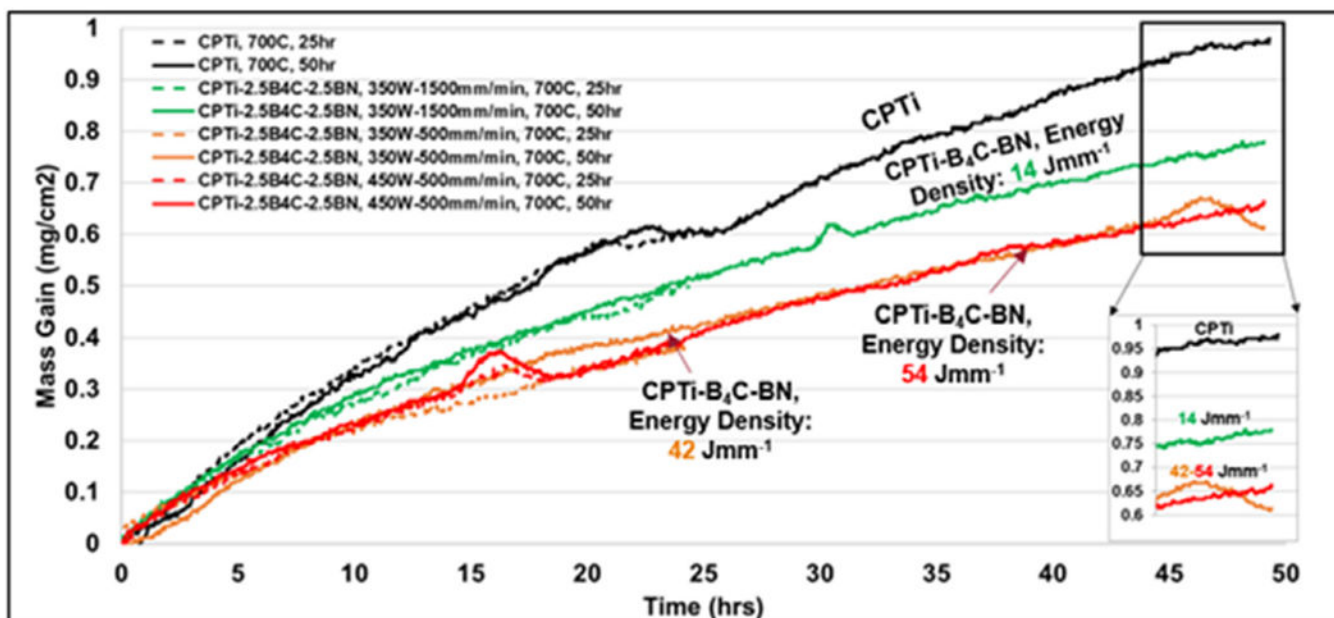
Fig. 8.
Thermogravimetric curves of each composition and processing parameters for both 25hrs.
and 50hrs at 700 °C in air. Note: dashed curves represent the 25hr runs.
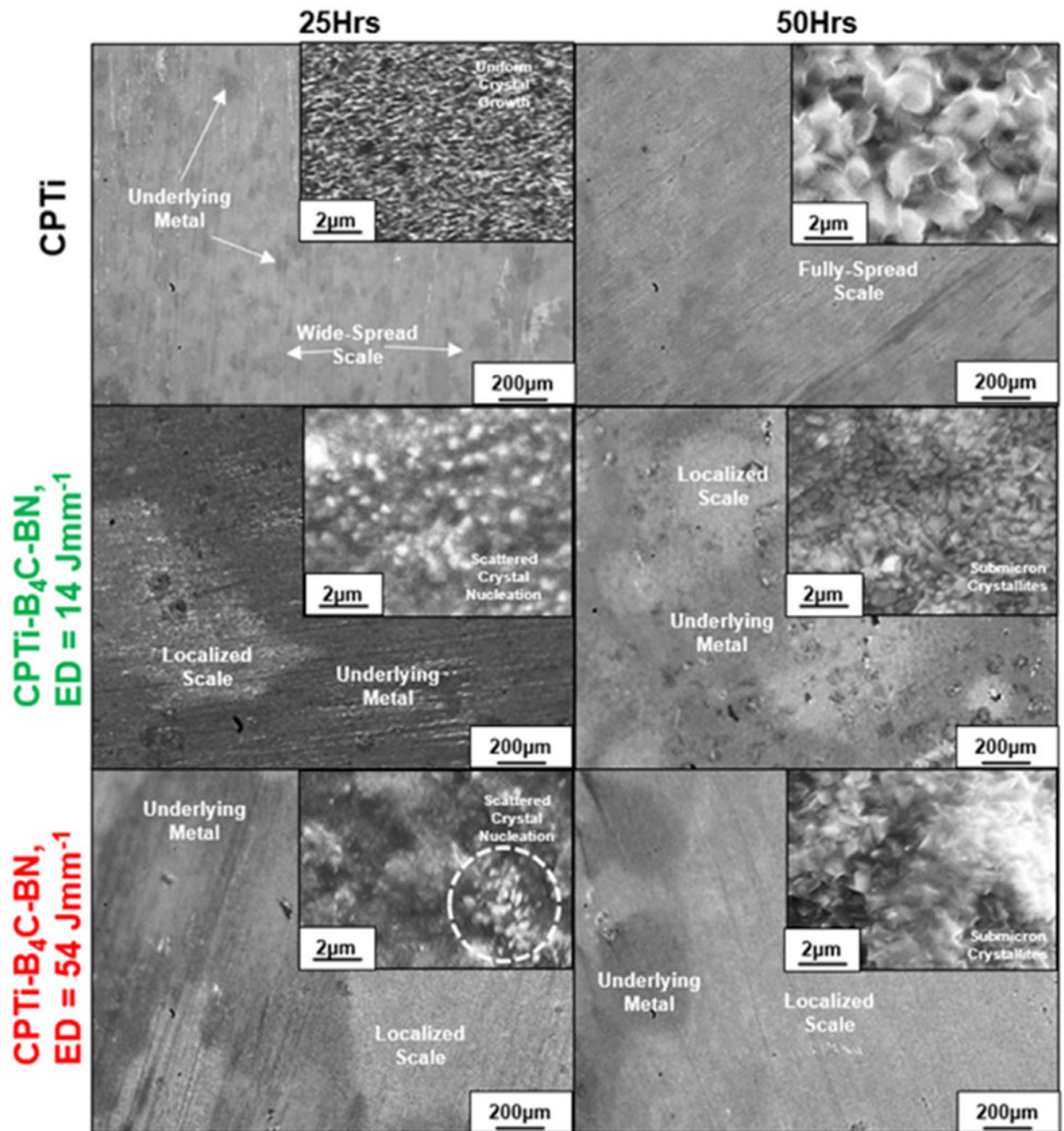
Fig. 9.
Comparison of oxide scales on surface of both CPTi and CPTi-B₄C-BN compositions at different input energies and at each time point. Inset images are the same sample at high magnification.
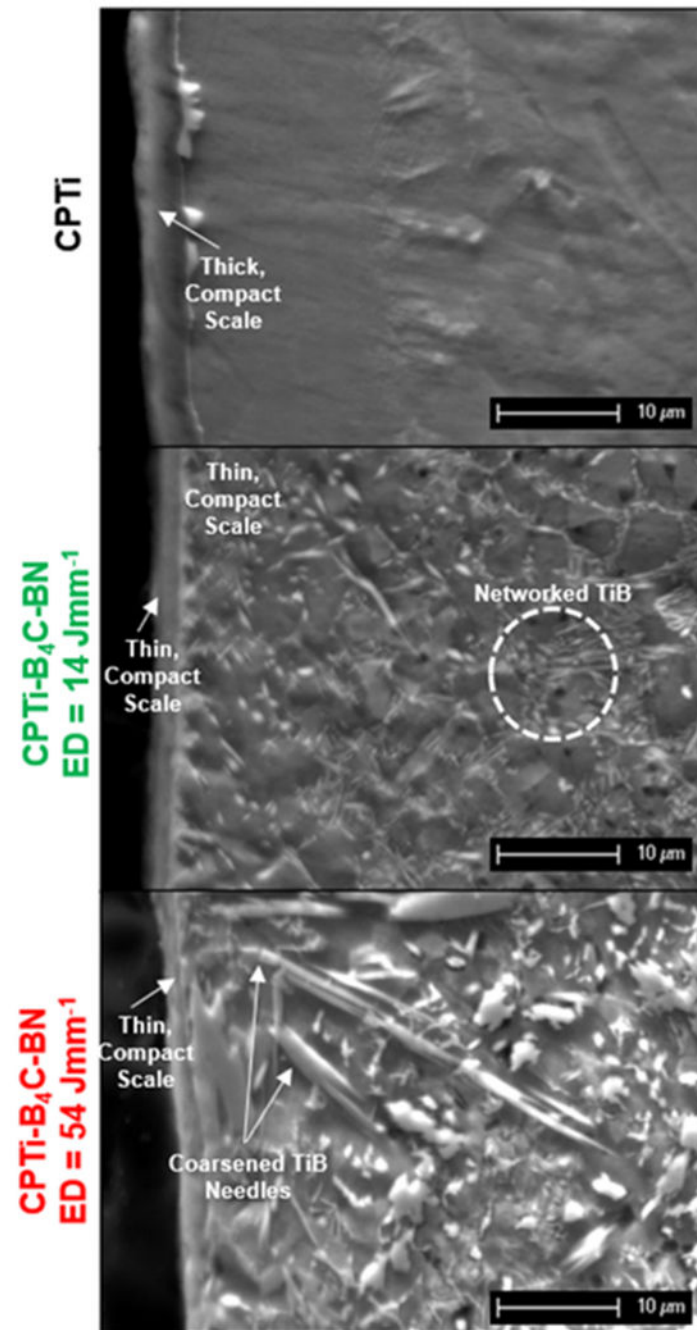
Fig. 10.
Comparison of oxide scale cross sections of both the CPTi and CPTi-B$_4$C-BN compositions at different input energies.
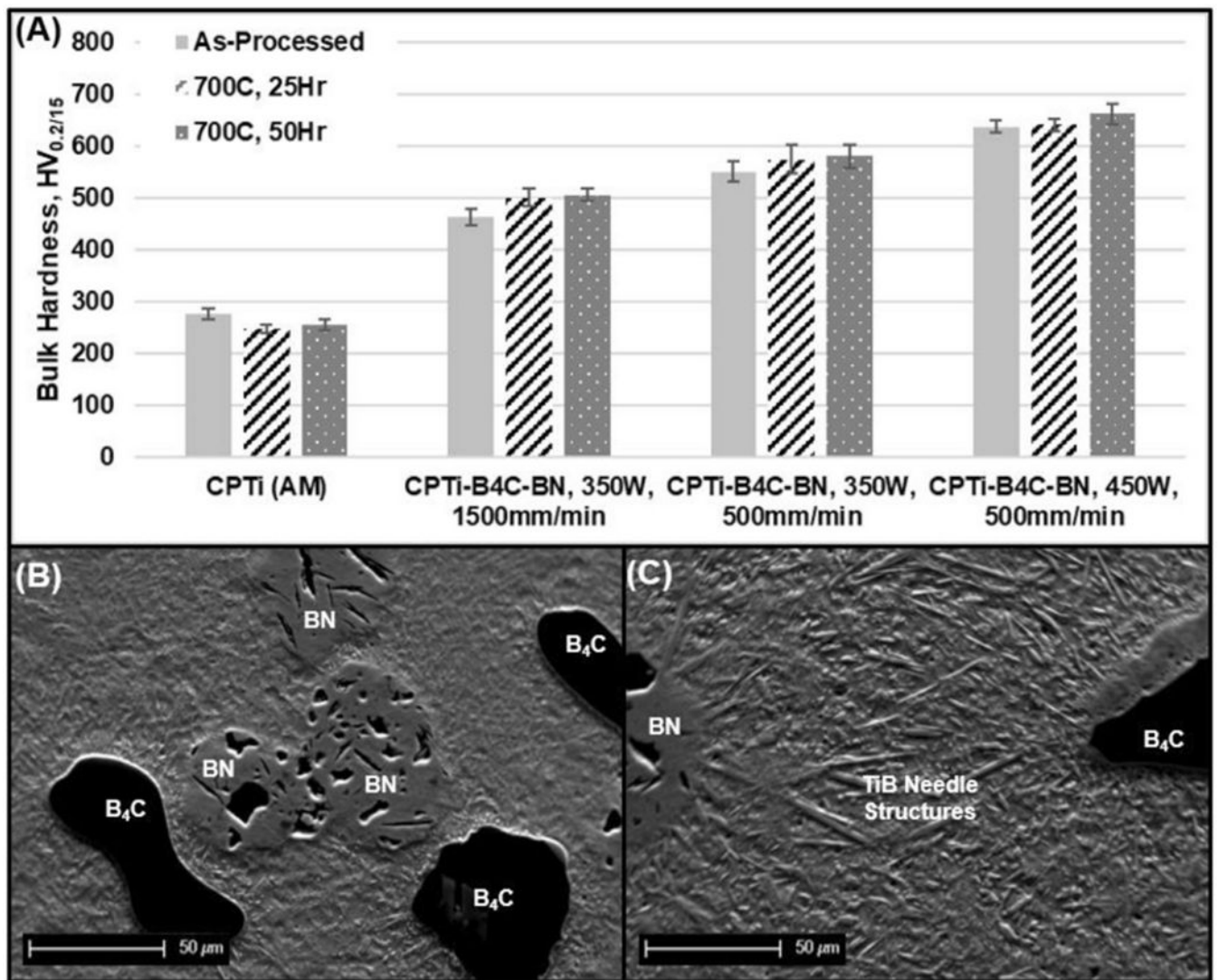
Fig. 11.
Hardness and microstructures of as-oxidized specimens. (**A**) Hardness of each composition and process parameter set after both 25hr and 50hr tests at 700 °C. (**B**) Microstructure of CPTi-B_4C-BN composition processed at 14 Jmm^{-1}. (**C**) Microstructure of CPTi-B_4C-BN composition processed at 54 Jmm^{-1}.

Table 1

Processing parameters for different single-tracks. Original parameters were centered around 350–450 W and 500–1500 mm/min scanning speed.

Parameter Set	Laser Power (W)	Scanning Speed (mm/min)	Hatch Spacing (mm)	Laser Energy Density (Jmm^{-1})
1	350	500	0.8[*]	42
2		1000		21
3		1500		14
4	400	500		48
5		1000		24
6		1500		16
7	450	500		54
8		1000		27
9		1500		18

[*] Corresponds to ~33% hatch overlap for 1.2 mm laser spot size on each track.

Author Manuscript

Author Manuscript

Author Manuscript

Author Manuscript

Table 2

Oxidation fitting parameters for each of the printed compositions.

T(°C)	Composition	Oxidation Characteristics	Fit Parameters for 25hr and 50hr Runs		
			*K_p	n	R^2 Value
700 °C	**CPTi**	Parabolic-Breakaway	$6.55e^{-2} \pm 1.77e^{-2}$	1.38 ± 0.1	0.99
	CPTi-B$_4$C-BN ED = 14		$5.53e^{-2} \pm 4.24e^{-4}$	1.44 ± 0.001	0.99
	CPTi-B$_4$C-BN ED = 42		$2.95e^{-2} \pm 6.36e^{-4}$	1.22 ± 0.04	0.97–0.99
	CPTi-B$_4$C-BN ED = 54		$4.35e^{-2} \pm 4.03e^{-3}$	1.39 ± 0.09	0.99

*
for linear kinetics (n = ~1) fit units of K_p (mg*cm^{-2}s^{-1}), whereas parabolic kinetic fit (n = ~2) units of K_p (mg^{2}cm^{-4}s^{-1}).